MTLA 40 (2025) 102409

Contents lists available at ScienceDirect

Materialia

journal homepage: www.elsevier.com/locate/mtla

Full Length Article

Whitlockite can be a substrate for apatite growth in simulated body fluid

Luke Hunter [a,b,*], Ryo Torii [c], Gaetano Burriesci [c,d], Sergio Bertazzo [a,e,**]

[a] Department of Medical Physics & Biomedical Engineering, University College London, London WC1E 6BT, UK
[b] Institute of Cardiovascular Science, University College London, London WC1E 6BT, UK
[c] Department of Mechanical Engineering, University College of London, London WC1E 6BT, UK
[d] Bioengineering Group, Ri.MED Foundation, Palermo 90133, Italy
[e] London Centre for Nanotechnology, University College London, London WC1E 6BT, UK

ARTICLE INFO

Keywords:
Biomineralisation
Calcification
Phase transformations
Crystallisation
SBF

ABSTRACT

Calcium phosphates are the predominant type of mineral in humans. They are essential for the formation of bones and teeth but can also deposit in diseased tissues. Whitlockite, a calcium phosphate mineral, is almost exclusively found in diseased calcified lesions. Despite its significance, the crystal growth mechanisms of whitlockite under physiological conditions are poorly understood. To investigate this, we conducted a constant composition experiment and applied a growth kinetics model to study the growth of whitlockite and hydroxyapatite nanoparticles in simulated body fluid. Contrary to our expectations, whitlockite did not dissolve in the undersaturated simulated body fluid. Instead, whitlockite nanoparticles served as a substrate for the formation of poorly-crystalline apatite, resulting in increased particle size. Our findings may help explain the colocalisation of whitlockite particles and large poorly-crystalline apatite lesions in human diseases.

1. Introduction

Bones are hierarchical structures composed of calcium phosphate minerals enmeshed within and around collagen fibres [1]. The predominant solid phase of calcium phosphate in bones is carbonate-substituted hydroxyapatite, also known as calcium-deficient hydroxyapatite, and is often simply referred to as bone apatite [1,2]. While bone apatite's fundamental structure is related to that of stoichiometric hydroxyapatite, which has the chemical formula $Ca_5(PO_4)_3(OH)$ and a predominantly hexagonal unit cell [2,3], bone apatite differs in composition due to ionic substitutions. It generally contains impurities such as 3–6 wt % carbonate and ~0.5 wt % magnesium and sodium, among others, which contribute to its calcium-deficient nature [2].

Carbonate-substituted hydroxyapatite is also present in human disease. When discovered it is known as pathological calcification and is a hallmark of several conditions, including cardiovascular calcification [4–6], breast cancer [7], macular degeneration [8], Alzheimer's [9], and kidney stones [10].

Another notable calcium phosphate mineral is whitlockite. Whitlockite is special because it is found in pathological calcification and not in bone [11], often with a particulate morphology [4,5,7,8]. Stoichiometric whitlockite has the chemical formula $Ca_9Mg(HPO_4)(PO_4)_6$ and has a rhombohedral unit cell which typically leads to cube-like morphology [12]. Due to its structural and compositional similarities to carbonate-substituted hydroxyapatite, early studies misidentified its presence in healthy bone, leading to misinterpretations [11].

The formation of bone and pathological calcification is believed to occur via the agglomeration of vesicles loaded with calcium and phosphate, followed by the release of their contents [13–17]. However, many details of this process remain unresolved, such as the role whitlockite particles play in the progression of pathological calcification.

To better understand calcification, the growth of these minerals is often analysed through acellular *in vitro* experiments and mathematical models. Simulated body fluid (SBF) is commonly used to mimic the physiological conditions relevant to calcification [18]. SBF replicates the ionic salt composition of human blood plasma [18]. Both SBF and blood serum are supersaturated with respect to hydroxyapatite [19,20], making SBF a metastable solution that typically precipitates carbonate-substituted hydroxyapatite [18].

In SBF, carbonate-substituted hydroxyapatite primarily forms through the conversion of amorphous calcium phosphate (ACP), which nucleates in the solution first [21,22]. Once formed,

* Corresponding author at: Institute of Cardiovascular Science, University College London, London WC1E 6BT, UK
** Corresponding author.
E-mail addresses: ucemlwh@ucl.ac.uk (L. Hunter), s.bertazzo@ucl.ac.uk (S. Bertazzo).

https://doi.org/10.1016/j.mtla.2025.102409
Received 5 February 2025; Accepted 11 April 2025
Available online 11 April 2025

carbonate-substituted hydroxyapatite continues growing through the deposition and crystallisation of ACP layers [22–25]. Hydroxyapatite growth is slow because it requires the incorporation of large growth units called Posner clusters ($Ca_9(PO_4)_6$, ~0.8 nm) [21,22,26,27]. Consequently, the growth rate is limited by the incorporation rate of these molecules rather than ion diffusion to the crystal surface [27]. Growth mechanisms of whitlockite are comparatively poorly understood. To our knowledge, only one study has investigated the growth kinetics of whitlockite in aqueous solution, but this was not performed in a physiologically relevant solution [28]. Apatite formation on other calcium phosphate ceramics in SBF, such as tricalcium phosphate (TCP), has also been shown to depend on factors such as porosity and surface area [29,30].

Mean-field mathematical models of crystal growth, often used in materials science, typically assume concentration gradients occur only near the crystal surface [31]. Modelling hydroxyapatite crystal growth in SBF is challenging due to the complexity of SBF's chemistry and hydroxyapatite's growth mechanism. Additionally, no models have been developed for whitlockite growth kinetics in aqueous solutions. Most mean-field models of hydroxyapatite growth assume that (i) diffusion, rather than incorporation at the interface, is rate-limiting [32] (ii) only two species are diffusing [27,33,34]. In contrast, SBF typically contains ten reagents that can dissociate and recombine into many diffusing species [20], making it a multicomponent solution. The diffusivities of species in multicomponent physiological solutions differ significantly from those in simpler solutions due to strong interactions between oppositely charged species [35].

In this study, we investigate the growth of hydroxyapatite and whitlockite seed nanoparticles with physiologically relevant morphologies in SBF. We also apply a multicomponent growth model, that considers both diffusion rates and incorporation rates at the interface, to gain a better understanding of the growth processes.

2. Materials and methods

2.1. Nanoparticles

2.1.1. Whitlockite nanoparticles

We synthesised whitlockite nanoparticles following an established protocol [12]. A capped, jacketed beaker containing 500 ml of deionised water was heated to 80 °C. To this, 3.79 g of magnesium hydroxide ($Mg(OH)_2$) and 13.71 g of calcium hydroxide ($Ca(OH)_2$) were added. Subsequently, 500 ml of 0.5 mol dm^{-3} phosphoric acid was introduced into the mixture at a controlled rate of 12.5 ml min^{-1} while being vigorously stirred using a magnetic stirrer. The reaction mixture was maintained for 24 h from the initial addition of phosphoric acid. Following this period, the mixture was allowed to cool to room temperature over 4 h. The resulting mixture was then filtered through 0.22 μm filter paper and washed with deionised water. The agglomerated wet powder left on the filter paper was dried at 37 °C for 3 days.

2.1.2. Hydroxyapatite nanoparticles

Hydroxyapatite particles were purchased from Sigma-Aldrich (catalogue no. 677418). These particles are polycrystalline [36] and have spherulitic morphologies resembling calcified particles found in the body [5].

2.2. XRD

To confirm our seed crystals were whitlockite we used X-ray diffraction (Stoe STADI-P, Germany). The X-ray radiation used for the analysis was Cu Kα1, operating at 40 kV and 30 mA, with a wavelength of 1.5406 Å. The scanning range for the 2θ angles was set from 5 ° to 60.44 °, with a step size of 0.495 ° Each step was measured for a duration of 10 s. A baseline intensity profile was defined using a spline polynomial to correct the raw intensity data.

2.3. Laser nanoparticle tracking

Whitlockite nanoparticles were thoroughly mixed with water and the resulting mixture was ultrasonicated for 6 min. Following ultrasonication, the mixture was introduced into a laser nanoparticle tracking system (NanoSight, UK) for analysis. The frame rate was maintained at 25 frames per second, capturing a total of 1499 frames. The liquid temperature was 22 °C, with an assumed water viscosity of 1.0 cP. The concentration of particles was 7.89×10^9 particles ml^{-1}.

2.4. Constant composition crystal growth experiment

We designed an experiment to grow seed crystals under constant composition conditions (Fig. 1). We thoroughly mixed 2 mg of nanoparticles into 100 μl of deionised water, then pipetted 0.25 μl of this mixture into a dialysis pot (Thermo-Fisher catalogue no. 69590) containing 100 μl of SBF made according to ISO 23317:2014. This yielded 5 μg of seed nanoparticles in the pot. The dialysis pot had a semipermeable membrane at its base, designed to prevent molecules greater than 20 kDa (~1.78 nm [37]) from passing through it. Most pertinent diffusing species in ISO SBF (Table 1) are much smaller than this [32,38] and the largest, the TRIS buffer molecule, is <0.8 nm [26]. Previous studies on hydroxyapatite precipitation involving membranes with pore sizes significantly larger than the diffusing species indicate that the membranes do not affect the precipitation process [38].

The dialysis pot was suspended with parafilm inside a 50 ml plastic container holding 42 ml of ISO SBF. Parafilm did not cover the entire container top, and the lid was only partially on to allow for CO_2 equilibration with the atmosphere. The base of the pot was submerged in ISO SBF in the container. If the seed crystals grew or dissolved, they would alter the ion concentration of the liquid around them. Since species can diffuse across the membrane between the liquid in the pot and the larger volume of SBF in the container, a constant composition could be maintained. The mixtures were incubated at 37 °C on an orbital shaker table.

If 5 μg of hydroxyapatite seed crystals grew in mass by 500 % (typical increases observed in hydroxyapatite seed particle growth are 100–250 % [25]), 10 μg of calcium would be required from the SBF. The total mass of calcium in 42 ml of ISO SBF is 4.21 mg. A reduction of 10 μg would yield a calcium concentration change of $\sim6\times10^{-6}$ mol dm^{-3} in the SBF. This is equivalent to the accuracy that traditional constant composition studies employing calcium ion probes achieve [39]. Hence, we consider our experimental system to be at constant composition.

2.5. Growth kinetics model

We applied a recently derived model of spherulitic crystal growth in multicomponent solutions [40], used in the popular materials equilibrium software Thermo-Calc [41]. The radial growth rate $\frac{dr}{dt}$ is given by

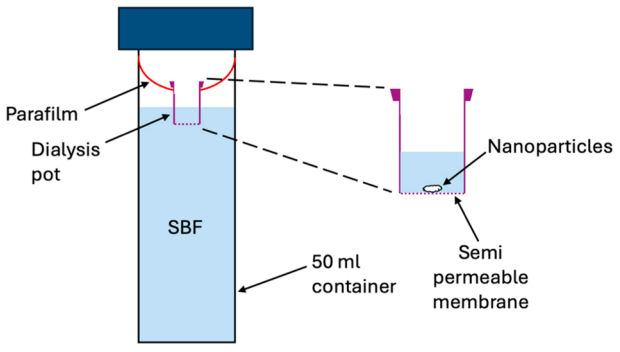

Fig. 1. Schematic of the constant composition study undertaken to study seed particle growth in SBF.

Table 1
Computed parameters used for the growth kinetics model.

Species	$x_{i,solution}$	$a_{i,solution}$	D_i^0 ($m^2\ s^{-1}$)	$\Delta x_{i,hydroxyapatite}$	$\Delta x_{i,whitlockite}$	L_{ii} ($m^2\ mol\ J^{-1}\ s^{-1}$)
Cl^-	1.42E-01	1.07E-01	2.55E-09	−1.42E-01	−1.42E-01	1.41E-13
Na^+	1.36E-01	1.02E-01	1.70E-09	−1.36E-01	−1.36E-01	9.01E-14
$TRIS^-$	3.09E-02	3.21E-02	8.23E-10	−3.09E-02	−3.09E-02	9.87E-15
K^+	4.81E-03	3.62E-03	2.44E-09	−4.81E-03	−4.81E-03	4.56E-15
Ca^{2+}	2.10E-03	6.70E-04	5.07E-10	5.53E-01	5.27E-01	4.13E-16
Mg^{2+}	1.19E-03	3.78E-04	4.40E-10	−1.19E-03	5.76E-02	2.02E-16
HPO_4^{2-}	4.50E-04	1.44E-04	4.90E-10	−4.50E-04	5.84E-02	8.55E-17
SO_4^{2-}	3.75E-04	1.20E-04	5.54E-10	−3.75E-04	−3.75E-04	8.06E-17
HCO_3^-	1.59E-04	1.19E-04	1.28E-09	−1.59E-04	−1.59E-04	7.85E-17
OH^-	7.99E-07	6.01E-07	6.45E-09	1.11E-01	−7.99E-07	2.00E-18
H^+	5.30E-08	3.98E-08	1.10E-08	−5.30E-08	−5.30E-08	2.26E-19
PO_4^{3-}	2.51E-08	1.92E-09	7.70E-09	3.33E-01	3.53E-01	7.49E-20

Eq. (1) [40].

$$\frac{dr}{dt} = \frac{1}{r}\frac{2\sigma V_m}{\left(\frac{V_m}{rM_{int}} + \Delta x^T L^{-1}\Delta x\right)}\left(\frac{1}{r_c} - \frac{1}{r}\right) \tag{1}$$

Where r is the current radius of the crystal (m), V_m is the molar volume of the crystal phase ($m^3\ mol^{-1}$), σ is the interfacial energy between the crystal and solution phases ($J\ m^{-2}$), M_{int} is interfacial mobility [42] ($m^4\ J^{-1}\ s^{-1}$), Δx is a column vector of the difference in component mole fraction between solution and crystal phases (dimensionless) [43], Δx^T is its transpose, r_c is the critical radius at which point the crystal is energetically stable and is expected to grow (m), and L is the symmetrical Onsager phenomenological coefficients matrix [44] ($m^2\ mol\ J^{-1}\ s^{-1}$).

2.5.1. Diffusing components

In diffusing aqueous solutions, components are often taken to be the added neutral salts, such as NaCl [35,45,46]. However, stoichiometric hydroxyapatite and whitlockite are conveniently expressed according to their constituent ions. Hence, we consider the diffusing components to be ions. Previous work shows that phase transformations of calcium phosphate minerals in solutions can be modelled assuming growth units are individual ions [32]. Using Visual MINTEQ [47], we determined the possible reactions in the system and the concentrations and activities of the aqueous species. Inputs included the nominal concentrations of ions of ISO SBF, atmospheric CO_2 partial pressure, a fixed pH of 7.4, and equilibrium constants from the software database. This yielded a list of 56 aqueous species.

Ions with concentrations $<5 \times 10^{-4}$ mol dm^{-3} have a negligible impact on diffusion in aqueous phosphate solutions and can be ignored, except any species required to balance the first dissociation reactions of solutes [46]. Since whitlockite contains PO_4^{3-}, we included this ion despite its negligible concentration, resulting in 12 ions (Table 1).

2.5.2. Onsager phenomenological matrix

SBF is a dilute solution, so we assume that the ion Onsager phenomenological matrix is diagonal [45,46,48]. The diagonal coefficients are found using Eq. (2) [45,46,48].

$$L_{ii} = \frac{x_i D_i^0}{RT} \tag{2}$$

Where x_i is the mole fraction of the species in the solution (dimensionless), D_i^0 is the limiting diffusivity of that species ($m^2\ s^{-1}$), R is the universal gas constant ($J\ mol^{-1}\ K^{-1}$), and T is temperature (K). The limiting diffusivity D_i^0 ($m^2\ s^{-1}$) is calculated using the molar conductance relation (Eq. (3)) [45,46].

$$D_i^0 = \frac{RT}{F^2}\frac{\lambda_i^0}{{z_i}^2} \tag{3}$$

Where F is Faraday's constant ($C\ mol^{-1}$), λ_i^0 is the limiting molar conductance of the species ($S\ m^2\ mol^{-1}$) and z_i is its charge (dimensionless). Using limiting molar conductance values [49–53] and charges, we calculated the limiting diffusivities and diagonal coefficients of the Onsager matrix (Table 1).

2.5.3. Crystal growth parameters

We calculated the difference in component mole fractions between solution and crystal phases for hydroxyapatite and whitlockite (Table 1). Molar volumes were derived from the molar mass and density of the crystal phase. The calculated molar volumes for hydroxyapatite and whitlockite were 3.25×10^{-4} and 6.71×10^{-4} $m^3\ mol^{-1}$, respectively. Interfacial energy, difficult to measure experimentally, was estimated to be between 10–120 mJ m^{-2} for both minerals [54]. As in previous studies of interface-limited crystal growth, we treated the interfacial mobility as an adjustable parameter found by fitting the model to experimental growth data [33,34].

2.5.4. Critical radius and supersaturation

The critical radius for hydroxyapatite and whitlockite was calculated using Eq. (4) [31].

$$r_c = \frac{2\sigma v_{at}}{kTln(S)} \tag{4}$$

Where v_{at} is the atomic or molecular volume of the crystal phase (m^3) [54], k is Boltzmann's constant ($J\ K^{-1}$), and S is supersaturation of the crystal phase with respect to the solution (dimensionless). Atomic volume of the crystal phase was determined by dividing the molar volume by Avogadro's number. The calculated atomic volumes for hydroxyapatite and whitlockite were 5.4×10^{-28} and 1.12×10^{-27} m^3, respectively.

Supersaturation was determined using Eq. (5) [55].

$$S = \frac{\prod_{i=1} {a_i}^{v_i}}{K_{sp}} \tag{5}$$

Where a_i is the activity of an ion in the solution (dimensionless), v_i is its stoichiometric number in the crystal's full unit cell formula (dimensionless), and K_{sp} is the solubility product of the crystal phase (dimensionless).

If SBF experiments are conducted in the presence of atmospheric partial pressure CO_2, carbonate-substituted calcium hydroxyapatite is precipitated [56]. In ISO SBF, the carbonate substitution is approximately 3 wt % [56]. The solubility product of carbonate-substituted hydroxyapatite is lower than that of stoichiometric hydroxyapatite [57,58].

Some precipitation models incorporate these solubility products in their calculations of supersaturation [27]. Others, which identified carbonate substitution in the hydroxyapatite that formed [25] or could not eliminate CO_2 from the solution [33,34,59], used values for

stoichiometric hydroxyapatite. Formulas for calculating the solubility product of carbonate-substituted hydroxyapatite are available [57], but the accuracy of the experimental techniques they were derived from has been questioned [58,60]. Moreover, empirical corrections are not available for the potentially significant cofactor effects of other substituted ions [19,61] and the size of the nucleated crystal could also affect supersaturation [19]. Given these complications, we followed previous works [25,33,34,59] and used parameters for bulk stoichiometric hydroxyapatite.

Ion activities were calculated by Visual MINTEQ (Table 1). Solubility products of hydroxyapatite and whitlockite were taken from experimental measurements [60,62,63] and adjusted for 37 °C using Eq. (6) [64].

$$\Delta G^{\Theta} = -RTln(K_{sp}) \tag{6}$$

The calculated K_{sp} values for hydroxyapatite and whitlockite were 7.5×10^{-122} and 4.48×10^{-110}, respectively. Calculated supersaturations were 4.42×10^{24} for hydroxyapatite and 1.24×10^{-67} for whitlockite.

Once the initial particle sizes and parameters were found, numerically solving Eqn. (1) yielded the expected particle radius over time.

2.6. TEM, SAED, and EDX

Nanoparticles were immersed in either SBF or deionised water for varying durations. Two independent samples were prepared for each immersion time point. After submersion, nanoparticles were extracted, triple washed with deionised water, and deposited on transmission electron microscope (TEM) grids. Sodium chloride precipitates in SBF upon drying and has a similar crystal morphology to whitlockite [65]. Washing redissolves sodium chloride and removes it from the sample [65]. A 2 nm carbon coating was applied to the samples prior to imaging (Leica EM ACE600, Germany). We used a JEM-2100Plus (Joel, Japan) TEM for obtaining images and selected area electron diffraction (SAED) patterns, and an X-max 80T (Oxford Instruments, UK) for energy-dispersive X-ray (EDX) spectra. Imaging was done at 200 kV and 108 μA. To further ensure that imaged particles were not sodium chloride, EDX was performed to identify elements present in regions of interest before imaging and SAED. No sodium chloride was detected in any sample. Elemental ratio measurements were calibrated using dry stoichiometric hydroxyapatite and whitlockite seed particles. When reported, elemental ratios were measured from a single representative immersed sample, with three surface points per sample averaged. Maximum deviations between measurements were <5 %.

Particle measurements were performed using Fiji [66], calculating equivalent radii from projected areas. Size distributions were pooled across both replicates, with at least 15 measurements collected in each condition prior to particle coalescence. Diffraction intensities and interplanar spacing were determined from SAED patterns using a radial average of pixel intensity away from the beam centre. Intensities were corrected in the same way as XRD data with crystallinity assessed via the full width half max (FWHM) peaks of the [2 1 1] and [1 2 1] planes in hydroxyapatite samples and the [2 2 6] plane in whitlockite samples.

3. Results

3.1. Whitlockite powder synthesis

A representative TEM image of freshly synthesised whitlockite powder particles is shown in Fig. 2A. The particles exhibit polyhedral morphologies, likely due to whitlockite's rhombohedral crystal unit cell [12]. The particle size distribution, measured using the nanoparticle tracking system, is presented in Fig. 2B The mode equivalent spherical radius of our whitlockite particles was found to be 24 nm, which is consistent with the 25 nm radius reported in previous work [12].

The X-ray diffractogram is shown in Fig. 2C. The peaks between 29.5

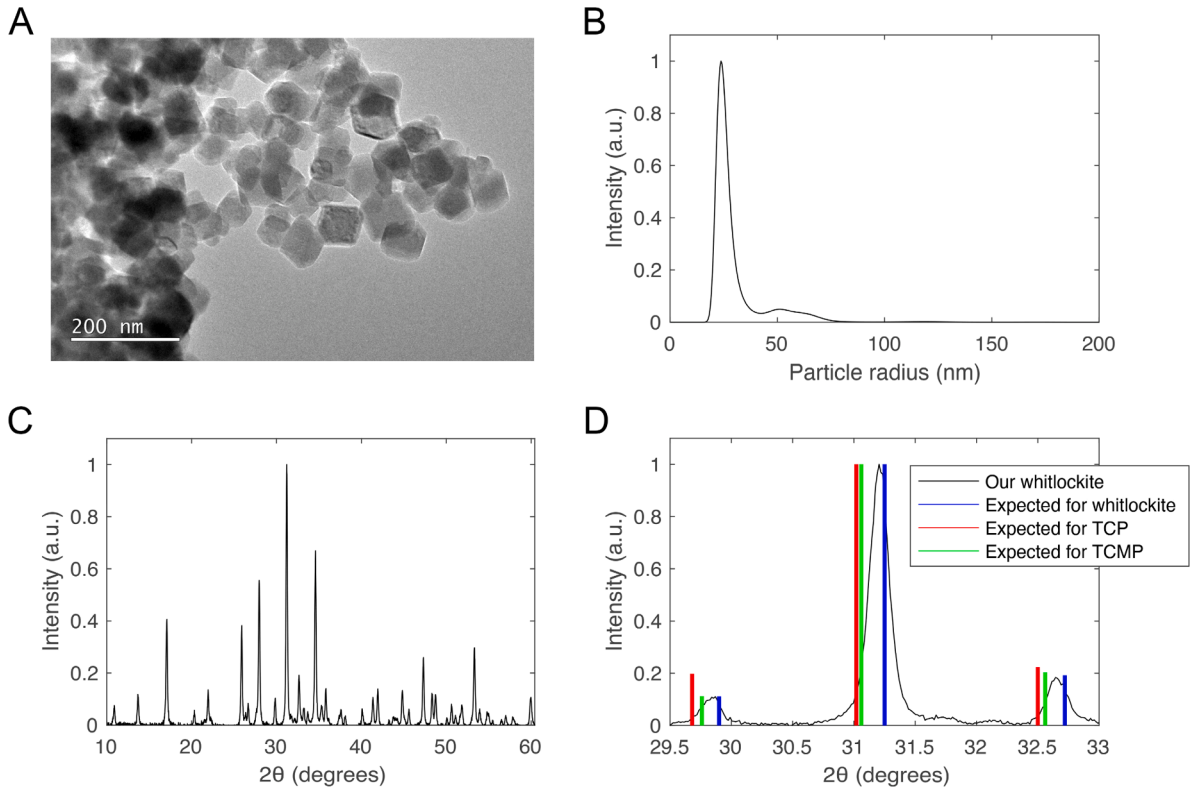

Fig. 2. Characteristics of synthesised whitlockite powder. (A) Representative TEM image of whitlockite powder particles. (B) Particle size distribution measured using the nanoparticle tracking system. (C) Measured XRD diffraction pattern of the powder sample. (D) Comparison of the measured XRD diffraction pattern between 29.5 and 33 ° to those obtained for whitlockite, tricalcium phosphate (TCP), and tricalcium magnesium phosphate (TCMP) samples from a previous study [12].

and 33 ° were compared to prior XRD data for whitlockite particles previously synthesised [12] and two similar calcium phosphate minerals: TCP and tricalcium magnesium phosphate (TCMP) [12] (Fig. 2D). The peak positions and intensities of the synthesised whitlockite are very similar to those of the previously produced whitlockite.

3.2. Particle size change after immersion

The particle sizes measured using TEM images of recovered seed particles after immersion in SBF are shown in Fig. 3A and 3B The equivalent radius of hydroxyapatite and whitlockite seed particles increased over time. The initial mean equivalent radius of hydroxyapatite and whitlockite seeds was 24 nm and 26 nm, respectively. After 19 days of immersion in SBF, the mean equivalent radius of hydroxyapatite and whitlockite seeds increased to 1773 nm and 40 nm, respectively. Hydroxyapatite seed particles were significantly larger than whitlockite seed particles by day 19, and the boundaries between the original seed particles were no longer discernible even by day 12. By this time, particles (Fig. 3C) had coalesced into much larger particles (Fig. 3D). Coalescence of whitlockite particles was not observed at any time.

3.3. Particle crystallinity and chemical composition after immersion

The diffraction intensities and corresponding interplanar spacing of samples immersed in SBF are shown in Fig. 4A and 4B Typical SAED patterns observed are shown in Fig. S1. The expected most intense peaks, hydroxyapatite [2 1 1] and [1 2 1] planes at 2.8135 Å (RRUFF ID: R060180 [67]) and whitlockite [0 2 10] plane at 2.8582 Å (RRUFF ID: R080052 [67]), were visible. The FWHM of the analysed peaks increased over time in both hydroxyapatite and whitlockite samples. At day 0, 5, and 12, the FWHM for hydroxyapatite samples was 0.1707, 0.3668, and 0.3099 a.u., respectively. By day 19, a peak could not be uniquely identified. At day 0 and 5, the FWHM for whitlockite samples was 0.082 and 0.24 a.u., respectively, and by day 19, a peak could not be

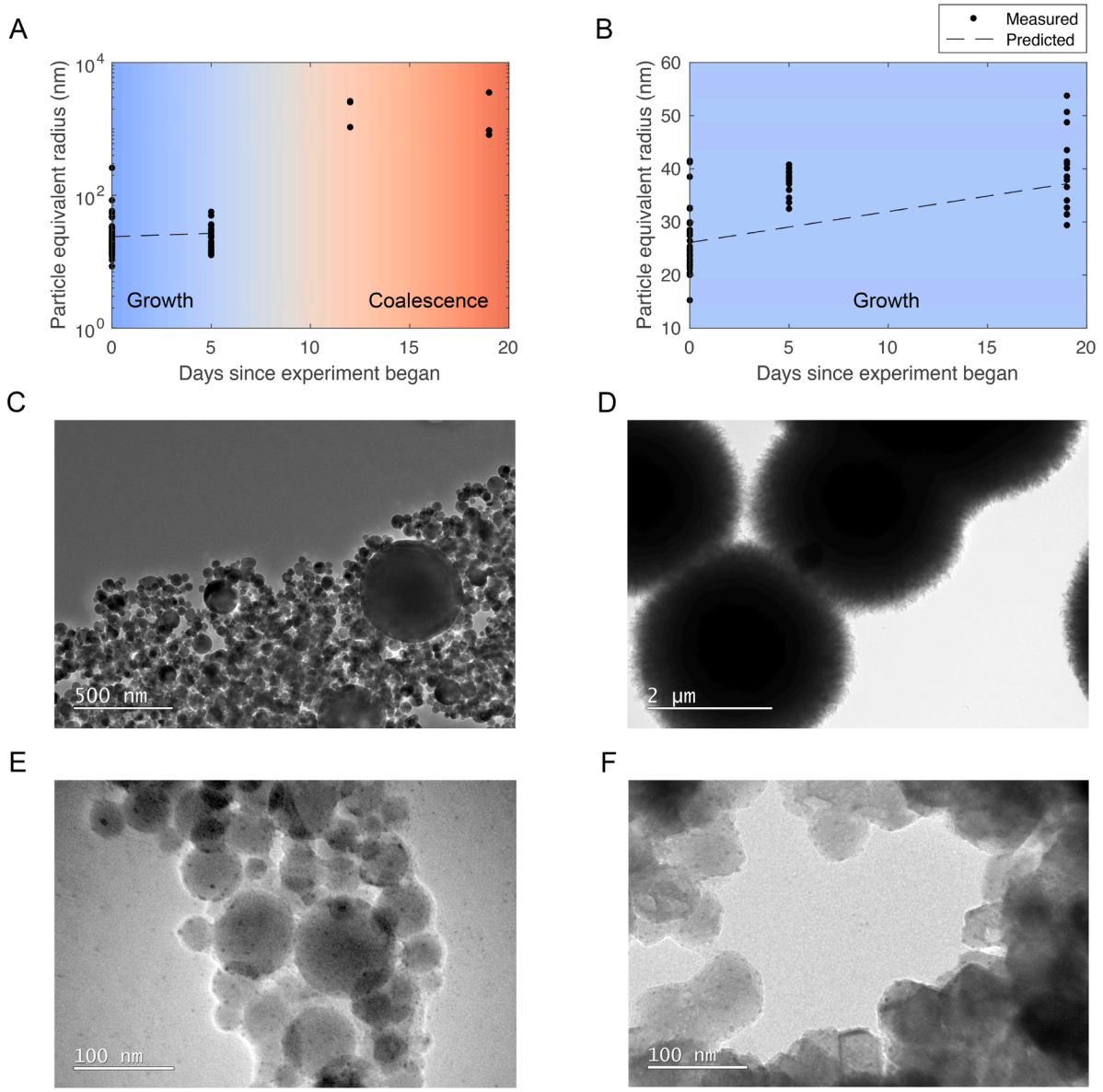

Fig. 3. Seed particle sizes after immersion in SBF. (A) Measured particle sizes after immersion in SBF of recovered hydroxyapatite seed particles. (B) Measured particle sizes after immersion in SBF of recovered whitlockite seed particles. The colour map illustrates the transition between growth and coalescence of hydroxyapatite particles observed. Particle size increase predicted using our crystal growth model is also shown. (C) Representative TEM image of fresh hydroxyapatite seed particles. (D) Representative TEM image of coalesced hydroxyapatite particles after 12 days of immersion in SBF. (E) Representative TEM image of hydroxyapatite seed particles after 5 days immersed in SBF. (F) Representative TEM image of whitlockite seed particles after 5 days immersed in SBF.

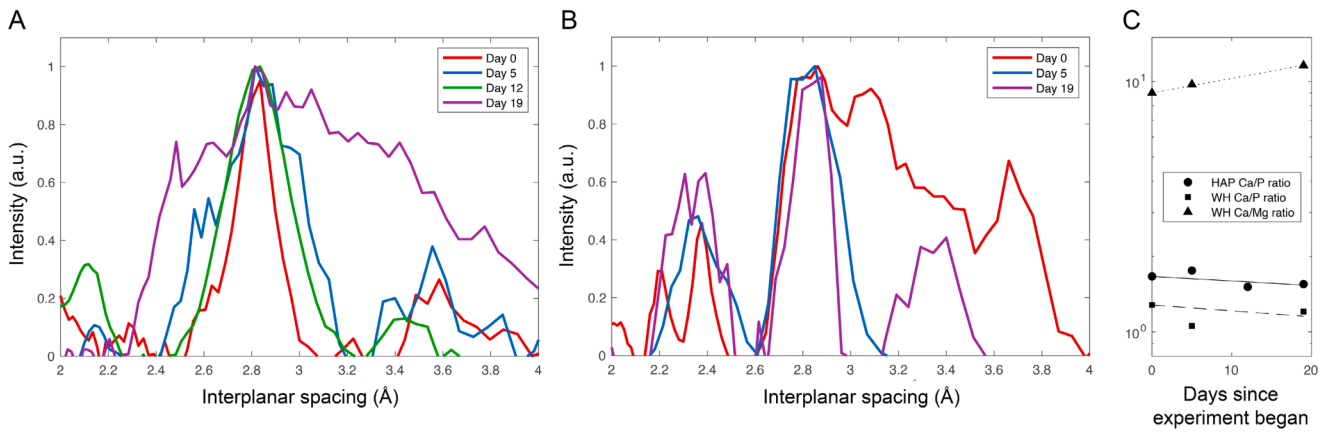

Fig. 4. Crystallinity and chemical composition of hydroxyapatite and whitlockite nanoparticles after immersion in SBF. (A) Measured diffraction pattern obtained from SAED of nanoparticle samples immersed in SBF for hydroxyapatite. (B) Measured diffraction pattern obtained from SAED of nanoparticle samples immersed in SBF for whitlockite. (C) Calcium to phosphorus ratios of hydroxyapatite and whitlockite samples, and calcium to magnesium ratio of whitlockite samples immersed in SBF with linear lines of best fit.

uniquely identified.

The ratio of calcium atoms to phosphorus atoms in hydroxyapatite and whitlockite samples immersed in SBF decreased over time (Fig. 4C). At day 0, the Ca/P ratio for hydroxyapatite and whitlockite was 1.66 and 1.28, respectively. By day 19, these ratios had decreased to 1.55 and 1.21, respectively. In contrast, the ratio of calcium to magnesium in whitlockite samples immersed in SBF increased over time (Fig. 4C). At day 0, the Ca/Mg ratio in whitlockite was 8.98, which increased to 11.6 by day 19. At days 12 and 19, hydroxyapatite samples immersed in SBF had detectable amounts of magnesium, yielding a Ca/Mg ratio of ~115.

4. Discussion

Hydroxyapatite and whitlockite particles maintained their approximately spherical shape before and after immersion in SBF, as shown in Figs. 2A, 3C, and 3E-F. At days 12 and 19, the hydroxyapatite particle size distribution significantly increased (Figs. 3A and D). Boundaries between individual particles were indistinguishable at these times, hence equivalent radii were taken of the large spherical structures visible (Fig. 3D). Two mechanisms are likely responsible for this particle size increase: (i) growth of individual seed particles and (ii) coalescence of growing seed particles.

Our calculations show that SBF is supersaturated with respect to hydroxyapatite, as shown previously [20]. Introducing seed particles into a supersaturated solution typically results in their growth, as observed in constant composition studies with hydroxyapatite seed particles [23–25]. Coalescence occurs due to high surface charge affinities of seed nanoparticles, leading to agglomeration and eventual formation of large, single particles [68]. This coalescence mechanism is a significant contributor to particle size increase over time [68]. We calculated that whitlockite has negative supersaturation in SBF and hence SBF is undersaturated with respect to whitlockite. This suggests that the seed particles would dissolve. Surprisingly, whitlockite particles increased in size over time.

The FWHM of characteristic peaks from electron diffraction are a comparative measure of nanoparticle crystallinity, with higher FWHM values indicating lower crystallinity [5]. By day 19, the expected positions of the characteristic peaks for both hydroxyapatite and whitlockite samples were too broad to discern (Fig. 4A-B), indicating a loss of long-range atomic order [5]. Crystallinity decreased over time for both hydroxyapatite and whitlockite particles in SBF. This has been observed in previous work and attributed to the growth of low-crystallinity carbonate-substituted hydroxyapatite on seed particle surfaces [23–25]. More recent studies without seed crystals showed that ACP forms first [21], crystallising slowly via several mechanisms [22]. In our experiment, crystallisation may be slower than the rate of deposition of additional ACP and may be exacerbated by the presence of TRIS buffer in ISO SBF which inhibits hydroxyapatite precipitation [25,69]. If ACP formation is faster than its crystallisation, measured crystallinity would decrease over time.

The Ca/P ratio of hydroxyapatite and whitlockite particles decreased over time, consistent with previous observations during hydroxyapatite seed growth in SBF [23–25]. This decrease was attributed to the growth of carbonate-substituted hydroxyapatite [23–25], which has a lower Ca/P ratio (1.3–1.5) [2]. ACP, which has a similar range of Ca/P ratios, is likely forming on particle surfaces, followed by a slow transformation to poorly crystalline carbonate-substituted hydroxyapatite. The detectable magnesium in hydroxyapatite samples at days 12 and 19 suggests magnesium incorporation by the crystal lattice. Carbonate-substituted hydroxyapatite and ACP can accommodate magnesium impurities [2] and have been observed in previous work with SBF [70]. The similar reduction in Ca/P ratios for whitlockite and hydroxyapatite indicates a similar growth process for both minerals. The increase in Ca/Mg ratio in whitlockite corroborates this as ACP and carbonate-substituted hydroxyapatite have a far lower magnesium content than whitlockite [2]. TEM images after 5 days of SBF immersion show growth morphologies and densities in whitlockite particles similar to those in hydroxyapatite particles (Figs. 3E and F), supporting our suggestion of ACP growth and slow crystallisation.

TEM images of seed particles after 5 days in SBF showed small dark spots on hydroxyapatite and whitlockite particles (Figs. 3E and F), absent in particles immersed in deionised water (Fig. S2). The appearance of these spots on particle surfaces in SBF suggests they are crystals of carbonate-substituted hydroxyapatite. This is consistent with previous studies where dark spots represented carbonate-substituted hydroxyapatite crystals nucleating on ACP seed particles [22,71]. These crystals appeared dark due to density-dependent contrast of the TEM (hydroxyapatite: 3.08 g cm^{-3}, whitlockite 3.13 g cm^{-3}, and ACP ~1.75 g cm^{-3} [22,72]) and mass-thickness effects, where these surface deposits add additional mass along the electron beam path. The size of these spots (mean size ~3 nm) is larger than the expected range of critical nuclei sizes (0.3–1.6 nm, see Supplementary Information) and consistent with previous observations of carbonate-substituted hydroxyapatite crystals (~5 nm) [68]. Additionally, TRIS molecules, which may adsorb onto the growing surfaces [24], are <0.8 nm [26]. Thus, we suggest that these spots are indeed crystals of carbonate-substituted hydroxyapatite that appear dark due to mass-thickness contrast.

Our crystal growth kinetics model assumes a spherical particle morphology, which is reasonable given the observed particle shape over time. We noted that whitlockite seed particles increased in size through

the growth of ACP and slow crystallisation to carbonate-substituted hydroxyapatite, in the same way as hydroxyapatite seed particles prior to coalescence. Therefore, we used hydroxyapatite parameters in our whitlockite growth model.

Figs. 3A and B show the predicted sizes of our hydroxyapatite and whitlockite seed particles, with M_{int} used as a fitting parameter. We only considered growth data from hydroxyapatite particles prior to coalescence, as our model does not account for this mechanism of size increase. Our model predicts that seed particle size increases linearly with time, consistent with previous studies of hydroxyapatite seed crystal growth in SBF [23,25]. The particle radial growth rate was determined to be 6.7×10^{-6} nm s^{-1} for both hydroxyapatite and whitlockite seed particles immersed in SBF.

Previous work indicates that the prism face of a hydroxyapatite crystal grows at $\sim 10^{-4}$ nm s^{-1} and its basal face at $\sim 10^{-2}$ nm s^{-1} in SBF [23,26]. These rates are several orders of magnitude higher than our measured growth rate, which may be attributed to the effects of TRIS buffer in our SBF, as previous work used less TRIS than ISO SBF [23,26]. TRIS inhibits the precipitation of hydroxyapatite in SBF [69] and can adsorb onto the growing faces of hydroxyapatite, mitigating growth [26].

Our model showed a good fit to both hydroxyapatite and whitlockite particle size increases using an M_{int} of 1.5×10^{-23} m^4 J^{-1} s^{-1}. Adjusting the range of σ values from 10–120 mJ m^{-2} significantly impacted r_c but had a negligible impact on the predicted crystal size. We found that M_{int} had a more substantial effect: an order of magnitude increase in M_{int} approximately doubled the predicted crystal size. This parameter is directly proportional to the velocity of a crystal boundary if growth is purely interface-limited and thus serves as an intrinsic measure of the ease of growth unit incorporation at the interface [42].

To our knowledge, few investigations of precipitation in aqueous solutions have considered the M_{int} parameter. An investigation of hydroxyapatite precipitation that included M_{int} in their model could not determine its value from their data [33,34]. For comparison, M_{int} values between certain crystalline phases in steels are typically 10^{-12}–10^{-17} m^4 J^{-1} s^{-1} from 300–1000 °C [42], and in some aluminium alloys, 10^{-15}–10^{-26} m^4 J^{-1} s^{-1} from 100–400 °C [73].

Our model only considers growth and not coalescence of the mineral. Coalescence significantly contributes to observed particle size increase at later times [68] and highlights the importance of accounting for crystal boundary collision [33,34], depletion of available space for growth [33,34], and particle surface charge leading to agglomeration.

It is interesting that partially crystalline layers of apatite grew on whitlockite. Given that SBF is undersaturated with respect to whitlockite, we would expect whitlockite to dissolve, releasing magnesium ions. Indeed at pH 7.4, the physiological pH to which SBF is buffered, and at body temperature (37 °C), hydroxyapatite is the thermodynamically favoured calcium phosphate phase over whitlockite [62]. Dissolution of magnesium from the whitlockite surface could locally elevate magnesium concentrations, which can slow, though not completely inhibit, the conversion of ACP to hydroxyapatite in SBF [2,70]. However, we observed that whitlockite acts as a substrate for apatite growth. The similarities to hydroxyapatite seed growth in crystallinity change, chemical composition, morphology, and particle size prediction over time suggest that if magnesium is being released, its inhibitory effect is negligible. The persistence of whitlockite under these conditions likely reflects stabilisation by a surface layer of partially crystalline apatite, preventing its dissolution.

An alternative scenario to consider is whether whitlockite seed particles first grew larger before the eventual formation of carbonate-substituted hydroxyapatite. While whitlockite growth in SBF is unexpected due to undersaturation, transient local changes in ionic composition or kinetic effects could theoretically stabilise its growth temporarily. However, our diffraction and chemical composition data (Fig. 4) show a progressive decrease in crystallinity and Ca/P ratio over time, which is consistent with the formation of ACP that eventually transforms to carbonate-substituted hydroxyapatite rather than continued whitlockite crystallisation. Hydroxyapatite and whitlockite seed particles also exhibited similar growth rates, and our growth model, which closely matches experimental observations, does not predict conditions that would support whitlockite particle growth. Although we cannot completely rule out transient whitlockite growth, the combined evidence strongly suggests that particle enlargement and morphological changes are driven by ACP deposition, followed by slow crystallisation into carbonate-substituted hydroxyapatite.

The possibility of a co-precipitated magnesium phosphate phase, such as newberyite [74], contributing to the increasing Ca/Mg ratio of whitlockite particles (Fig. 4C) also requires consideration. However, the very similar growth rates of hydroxyapatite and whitlockite particles in SBF suggest a common growth mechanism, supporting ACP-mediated whitlockite particle size increase. Additionally, the observed increase in peak broadening over time is indicative of decreasing crystallinity (Fig. 4B), consistent with ACP formation rather than the emergence of a crystalline magnesium phosphate phase. Further, such phases typically require phosphate and magnesium concentrations over 100 times greater than those present in SBF at pH 7.4 [74]. While the formation of a minor, amorphous magnesium phosphate phase cannot be entirely excluded, the data better support ACP formation as the main factor driving the observed increase in the Ca/Mg ratio of whitlockite seed particles.

Notably, no particle formation was observed in a pot immersed in SBF for 19 days without seed particles. This confirms that our system retains the crucial property of SBF test systems, where nucleation does not occur in the absence of apatite-specific substrates until after four weeks [18].

Our work shows that whitlockite can act as a substrate for the growth of poorly crystalline carbonate-substituted hydroxyapatite in an aqueous solution with a composition similar to human blood. Although simulated body fluid is metastable, with ACP and carbonate-substituted hydroxyapatite expected to form either homogeneously in solution or heterogeneously at interfaces [20], partial dissolution of whitlockite could release magnesium, which might theoretically inhibit nucleation. However, our results show that this dissolution does not prevent ACP or carbonate-substituted hydroxyapatite from nucleating on whitlockite seed surfaces. Whitlockite particles are found colocalised with bulk calcification, which is poorly crystalline carbonate-substituted hydroxyapatite [5], in calcifying heart valves [4,5], eyes [8], and some breast tumours [7]. These whitlockite particles may therefore act as a substrate for the growth of poorly crystalline carbonate-substituted hydroxyapatite in the body.

5. Conclusion

We investigated the growth of whitlockite and hydroxyapatite nanoparticles in SBF using a constant composition experiment and a multicomponent growth kinetics model. Contrary to our expectations, whitlockite nanoparticles did not dissolve in the undersaturated SBF but instead acted as a substrate for the formation of poorly-crystalline apatite. This growth resulted in an increase in particle size and a decrease in crystallinity over time. This may help explain the observed colocalisation of whitlockite particles with poorly-crystalline apatite in calcified lesions of the heart, eyes, and some breast tumours. This work provides evidence supporting a mechanism by which whitlockite particles could contribute to pathological calcification. Additional factors *in vivo*, such as cellular processes and organic components, likely play crucial roles in modulating this mechanism. Future research should explore whether the growth mechanisms observed here occur *in vivo* too.

Author contributions

L.H. conceived the paper, derived the models, analysed data, and wrote the manuscript. L.H. and S.B. conceived the experiments and data

analysis, performed the experiments, and revised the manuscript. S.B., R.T., and G.B. conceived the overall project and supervised.

Data and code availability

The data used can be found in the main text or supplementary materials.

Supplementary information

A supplementary information file has been included in this submission. It contains Supplementary Figures 1–4 and a derivation of how the expected visible size of a nucleus was determined.

Ethical approval

Not applicable

CRediT authorship contribution statement

Luke Hunter: Writing – review & editing, Writing – original draft, Visualization, Validation, Software, Resources, Project administration, Methodology, Investigation, Funding acquisition, Formal analysis, Data curation, Conceptualization. **Ryo Torii:** Supervision, Conceptualization. **Gaetano Burriesci:** Supervision, Conceptualization. **Sergio Bertazzo:** Writing – review & editing, Supervision, Conceptualization.

Declaration of competing interest

The authors declare that they have no known competing financial interests or personal relationships that could have appeared to influence the work reported in this paper.

Acknowledgements

We are grateful to Ben Blackburn and Holly Pearce at King's College London for their assistance with the NanoSight. We appreciate Martin Vickers at UCL for his support with the XRD. Additionally, we are grateful to Ecaterina Ware and Mahmoud Ardakani at Imperial College London for their help with the obtaining TEM, SAED, and EDX data. Luke Hunter acknowledges funding from British Heart Foundation grant FS/4yPhD/F/20/34134.

Supplementary materials

Supplementary material associated with this article can be found, in the online version, at doi:10.1016/j.mtla.2025.102409.

References

[1] N. Reznikov, et al., Fractal-like hierarchical organization of bone begins at the nanoscale, Science 360 (6388) (2018) eaao2189.
[2] M. Edén, Structure and formation of amorphous calcium phosphate and its role as surface layer of nanocrystalline apatite: implications for bone mineralization, Materialia 17 (2021) 101107.
[3] M.I. Kay, R.A. Young, A.S. Posner, Crystal structure of hydroxyapatite, Nature 204 (4963) (1964) 1050–1052.
[4] E. Tsolaki, S. Bertazzo, Pathological mineralization: the potential of mineralomics, Mater. (Basel) 12 (19) (2019) 3126.
[5] S. Bertazzo, et al., Nano-analytical electron microscopy reveals fundamental insights into human cardiovascular tissue calcification, Nat. Mater. 12 (6) (2013) 576–583.
[6] S. Bertazzo, et al., Cardiovascular calcification violet pearl, Lancet (2014).
[7] J.A.M.R. Kunitake, et al., Biomineralogical signatures of breast microcalcifications, Sci. Adv. 9 (8) (2023) eade3152.
[8] A.C.S. Tan, et al., Calcified nodules in retinal drusen are associated with disease progression in age-related macular degeneration, Sci. Transl. Med. 10 (466) (2018) eaat4544.
[9] E. Tsolaki, et al., Nuclear and cellular, micro and nano calcification in Alzheimer's disease patients and correlation to phosphorylated Tau, Acta Biomater. 143 (2022) 138–144.
[10] C. Thongprayoon, A.E. Krambeck, A.D. Rule, Determining the true burden of kidney stone disease, Nat. Rev. Nephrol. 16 (12) (2020) 736–746.
[11] F.A. Shah, Magnesium whitlockite – omnipresent in pathological mineralisation of soft tissues but not a significant inorganic constituent of bone, Acta Biomater. 125 (2021) 72–82.
[12] H.L. Jang, et al., Revisiting Whitlockite, the second most abundant biomineral in bone: nanocrystal synthesis in physiologically relevant conditions and biocompatibility evaluation, ACS Nano. 8 (1) (2014) 634–641.
[13] H.C. Anderson, The role of matrix vesicles in physiological and pathological calcification, Curr. Opin. Orthop. 18 (5) (2007) 428–433.
[14] T. Minashima, et al., Intracellular modulation of signaling pathways by Annexin A6 regulates terminal differentiation of chondrocytes*, J. Biol. Chem. 287 (18) (2012) 14803–14815.
[15] J. Mahamid, et al., Mapping amorphous calcium phosphate transformation into crystalline mineral from the cell to the bone in zebrafish fin rays, Proc. Natl. Acad. Sci. 107 (14) (2010) 6316–6321.
[16] J.D. Hutcheson, et al., Genesis and growth of extracellular-vesicle-derived microcalcification in atherosclerotic plaques, Nat. Mater. 15 (3) (2016) 335–343.
[17] M.A. Rogers, et al., Annexin A1–dependent tethering promotes extracellular vesicle aggregation revealed with single–extracellular vesicle analysis, Sci. Adv. 6 (38) (2020) eabb1244.
[18] T. Kokubo, H. Takadama, How useful is SBF in predicting *in vivo* bone bioactivity? Biomaterials 27 (15) (2006) 2907–2915.
[19] O. Söhnel, F. Grases, Supersaturation of body fluids, plasma and urine, with respect to biological hydroxyapatite, Urol. Res. 39 (6) (2011) 429–436.
[20] M. Bohner, J. Lemaitre, Can bioactivity be tested *in vitro* with SBF solution? Biomaterials 30 (12) (2009) 2175–2179.
[21] A. Dey, et al., The role of prenucleation clusters in surface-induced calcium phosphate crystallization, Nat. Mater. 9 (12) (2010) 1010–1014.
[22] K. He, et al., Revealing nanoscale mineralization pathways of hydroxyapatite using *in situ* liquid cell transmission electron microscopy, Sci. Adv. 6 (47) (2020) eaaz7524.
[23] K. Onuma, et al., Growth kinetics of hydroxyapatite crystal revealed by atomic force microscopy, J. Cryst. Growth 154 (1) (1995) 118–125.
[24] N. Kanzaki, et al., Direct growth rate measurement of hydroxyapatite single crystal by Moire Phase Shift interferometry, J. Phys. Chem. B 102 (34) (1998) 6471–6476.
[25] N. Spanos, et al., Seeded growth of hydroxyapatite in simulated body fluid, J. Mater. Sci. 41 (6) (2006) 1805–1812.
[26] A. Oyane, et al., Clustering of calcium phosphate in the system CaCl2−H3PO4−KCl−H2O, J. Phys. Chem. B 103 (39) (1999) 8230–8235.
[27] K. Onuma, Recent research on pseudobiological hydroxyapatite crystal growth and phase transition mechanisms, Prog. Cryst. Growth Charac. Mater. 52 (3) (2006) 223–245.
[28] M. Hamad, J.-C. Heughebaert, The growth of whitlockite, J. Cryst. Growth 79 (1) (1986) 192–197.
[29] T. Uchino, et al., Hydroxyapatite formation on porous ceramics of alpha-tricalcium phosphate in a simulated body fluid, J. Mater. Sci.: Mater. Med. 21 (6) (2010) 1921–1926.
[30] T. Uchino, et al., Hydroxyapatite-forming capability and mechanical properties of organic-inorganic hybrids and α-tricalcium phosphate porous bodies, J. Ceram. Soc. Japan 118 (1373) (2010) 57–61.
[31] J.W. Mullin, Crystallization, 4th ed., Butterworth-Heinemann, Oxford, UK, 2001.
[32] A. Carino, et al., Formation and transformation of calcium phosphate phases under biologically relevant conditions: experiments and modelling, Acta Biomater. 74 (2018) 478–488.
[33] A.T.C. Wong, J.T. Czernuszka, Transformation behaviour of calcium phosphate 1. Theory and modelling, Colloids Surf. A: Physicochem. Eng. Aspects 78 (1993) 245–253.
[34] A.T.C. Wong, J.T. Czernuszka, Transformation behaviour of calcium phosphate 2. Effects of various phosphorylated amino acids, Colloids Surf. A: Physicochem. Eng. Aspects 103 (1) (1995) 23–36.
[35] D.G. Leaist, P. Anderson, J.C. Elliott, Diffusion coefficients for the ternary system Ca(OH)2–H3PO4–water, J. Chem. Soc., Faraday Trans. 86 (18) (1990) 3093–3095.
[36] K.H. Müller, et al., The effect of particle agglomeration on the formation of a surface-connected compartment induced by hydroxyapatite nanoparticles in human monocyte-derived macrophages, Biomaterials 35 (3) (2014) 1074–1088.
[37] H.P. Erickson, Size and shape of protein molecules at the nanometer level determined by sedimentation, gel filtration, and electron microscopy, Biol. Proced. Online 11 (1) (2009) 32.
[38] Y.X. Ma, et al., Involvement of prenucleation clusters in calcium phosphate mineralization of collagen, Acta Biomater. 120 (2021) 213–223.
[39] L. Wang, et al., Constant composition studies verify the utility of the Cabrera−Vermilyea (C-V) model in explaining mechanisms of calcium oxalate monohydrate crystallization, Cryst. Growth Des. 6 (8) (2006) 1769–1775.
[40] M. Bonvalet-Rolland, T. Philippe, J. Ågren, Kinetic theory of nucleation in multicomponent systems: an application of the thermodynamic extremum principle, Acta Mater. 171 (2019) 1–7.
[41] J. Ågren, Q. Chen, Simplified growth model for Multicomponent systems - inclusion of PARA and NPLE conditions, J. Phase Equilibria Diffus. 43 (6) (2022) 738–744.
[42] M. Hillert, L. Höglund, Mobility of α/γ phase interfaces in Fe alloys, Scr. Mater. 54 (7) (2006) 1259–1263.
[43] J. Ågren, CALPHAD – An approach to predict microstructural stability, in: F. G. Caballero (Ed.), Encyclopedia of Materials: Metals and Alloys, Elsevier: Oxford, 2022, pp. 497–509.

[44] F.J. Spera, A.F. Trial, Verification of the Onsager reciprocal relations in a molten silicate solution, Science 259 (5092) (1993) 204–206.
[45] D. Leaist, Simplified theory of diffusion of mixed electrolytes with simultaneous chemical reactions. Application to glycine + HCl + H2O mixtures, J. Chem. Soc. Faraday Trans. 1: Phys. Chem. Condens. Phases 78 (10) (1982) 3069–3079.
[46] D.G. Leaist, Diffusion in dilute aqueous solutions of phosphoric acid. Verification of the limiting law for diffusion of weak electrolytes, J. Chem. Soc. Faraday Transactions 1: Phys. Chem. Condens. Phases 80 (11) (1984) 3041–3050.
[47] Gustafsson, J.P., Visual MINTEQ version 3.1. 2020.
[48] E.L. Cussler, Diffusion: Mass Transfer in Fluid Systems, 3rd ed., Cambridge University Press, Cambridge, UK, 2009.
[49] Robinson, R.A. and R.H. Stokes, Electrolyte Solutions. 2nd ed. 1962, New York, NY: Academic Press.
[50] R.G. Bates, H.B. Hetzer, Dissociation constant of the protonated acid form of 2-amino-2-(Hydroxymethyl)-1,3-propanediol [Tris-Hydroxymethyl)-Aminomethane] and related thermodynamic quantities from 0 to 50°, J. Phys. Chem. 65 (4) (1961) 667–671.
[51] M. Tomšič, et al., Conductivity of magnesium sulfate in water from 5 to 35°C and from infinite dilution to saturation, J. Sol. Chem. 31 (1) (2002) 19–31.
[52] E.N. Tsurko, et al., Conductivity of phosphoric acid, sodium, potassium, and ammonium phosphates in dilute aqueous solutions from 278.15 K to 308.15 K, J. Sol. Chem. 28 (8) (1999) 973–999.
[53] J.F. Talling, Electrical conductance — a versatile guide in freshwater science, Freshwater Rev. 2 (1) (2009) 65–78, 14.
[54] W. Wu, G.H. Nancollas, Determination of interfacial tension from crystallization and dissolution data: a comparison with other methods, Adv. Colloid Interf. Sci. 79 (2) (1999) 229–279.
[55] J. Moffitt Schall, A.S. Myerson, in: A.S. Myerson, D. Erdemir, A.Y. Lee (Eds.), Solutions and Solution Properties, in Handbook of Industrial Crystallization, Cambridge University Press, Cambridge, 2019, pp. 1–31.
[56] H.-M. Kim, et al., Composition and structure of the apatite formed on PET substrates in SBF modified with various ionic activity products, J. Biomed. Mater. Res. 46 (2) (1999) 228–235.
[57] A. Ito, et al., Solubility product of OH-carbonated hydroxyapatite, J. Biomed. Mater. Res. 36 (4) (1997) 522–528.
[58] H. Pan, B.W. Darvell, Effect of carbonate on hydroxyapatite solubility, Cryst. Growth Des. 10 (2) (2010) 845–850.
[59] W.J.E.M. Habraken, et al., Ion-association complexes unite classical and non-classical theories for the biomimetic nucleation of calcium phosphate, Nat. Commun. 4 (1) (2013) 1507.
[60] H.B. Pan, B.W. Darvell, Calcium phosphate solubility: the need for re-evaluation, Cryst. Growth Des. 9 (2) (2009) 639–645.
[61] Q. Liu, et al., The effect of excess phosphate on the solubility of hydroxyapatite, Ceram. Int. 40 (2) (2014) 2751–2761.
[62] M.C.F. Magalhães, M.O.G. Costa, On the solubility of whitlockite, Ca9Mg(HPO4)(PO4)6, in aqueous solution at 298.15 K, Monatshefte für Chemie - Chem. Monthly 149 (2) (2018) 253–260.
[63] N. Sahai, M.A. Schoonen, Accuracy of thermodynamic databases for hydroxyapatite dissolution constant, Astrobiology 20 (1) (2020) 157–160.
[64] J.N. Butler, Ionic Equilibrium: Solubility and pH Calculations, John Wiley & Sons, New York, NY, 1998.
[65] C. Drouet, Apatite formation: why it may not work as planned, and how to conclusively identify Apatite compounds, Biomed. Res. Int. 2013 (1) (2013) 490946.
[66] J. Schindelin, et al., Fiji: an open-source platform for biological-image analysis, Nat. Methods 9 (7) (2012) 676–682.
[67] B. Lafuente, et al., The power of databases: the RRUFF project, in: A. Thomas, D. Rosa Micaela (Eds.), Highlights in Mineralogical Crystallography, De Gruyter (O): Berlin, München, Boston, 2016, pp. 1–30.
[68] E.M. Rivera-Muñoz, et al., Growth of hydroxyapatite nanoparticles on silica gels, J. Nanosci. Nanotechnol. 11 (6) (2011) 5592–5598.
[69] M.T. Jahromi, G. Yao, M. Cerruti, The importance of amino acid interactions in the crystallization of hydroxyapatite, J. R. Soc. Interf. 10 (80) (2013) 20120906.
[70] F. Barrère, et al., Biomimetic calcium phosphate coatings on Ti6Al4V: a crystal growth study of octacalcium phosphate and inhibition by Mg2+ and HCO3−, Bone 25 (2, Supplement 1) (1999) 107S–111S.
[71] A. Lotsari, et al., Transformation of amorphous calcium phosphate to bone-like apatite, Nat. Commun. 9 (1) (2018) 4170.
[72] C. Combes, C. Rey, Amorphous calcium phosphates: synthesis, properties and uses in biomaterials, Acta Biomater. 6 (9) (2010) 3362–3378.
[73] P. Heugue, et al., Precipitation kinetics and evaluation of the interfacial mobility of precipitates in an AlSi7Cu3.5Mg0.15 cast alloy with Zr and V additions, Metals (Basel) 9 (7) (2019) 777.
[74] F. Tamimi, et al., Biocompatibility of magnesium phosphate minerals and their stability under physiological conditions, Acta Biomater. 7 (6) (2011) 2678–2685.